SIMULATIONS OF BINARY BLACK HOLES IN SCALAR FIELD COSMOLOGIES

A Thesis
Presented to
The Academic Faculty

by

Katharine Christina Tallaksen

In Partial Fulfillment
of the Requirements for the Degree
Master of Science in the
School of Computational Science and Engineering

Georgia Institute of Technology
August 2016

SIMULATIONS OF BINARY BLACK HOLES IN SCALAR FIELD COSMOLOGIES

Approved by:

Professor John Wise, Committee Chair
School of Physics
Georgia Institute of Technology

Professor Pablo Laguna, Advisor
School of Physics and School of
Computational Science and Engineering
Georgia Institute of Technology

Professor Deirdre Shoemaker
School of Physics and School of
Computational Science and Engineering
Georgia Institute of Technology

Professor Richard Vuduc
School of Computational Science and
Engineering
Georgia Institute of Technology

Date Approved: 19 July 2016

ACKNOWLEDGEMENTS

I would first like to thank my advisor, Professor Pablo Laguna, for his help, advice, and encouragement throughout my time at the Center for Relativistic Astrophysics. I would also like to thank my thesis committee for their insights and helpful comments: John Wise, Deirdre Shoemaker, and Richard Vuduc.

I also send acknowledgements and thanks to the Numerical Relativity group at Georgia Tech: Matt Kinsey, Juan Calderon-Bustillo, James Clark, Michael Clark, Brian Day, Karan Jani, Bhavesh Khamesra, Forrest Kieffer, and Kate Napier for their friendship and entertaining group meetings.

Finally, I would like to thank my parents, Robert and Tina; my brother, Peter; and the rest of my family, Bucky, Hank, Coco, and Zlatan; for their constant and unfailing support and love.

TABLE OF CONTENTS

LIST OF TABLES

LIST OF FIGURES

CHAPTER I

INTRODUCTION

Computation is now an integral part of many scientific fields. Scientific computing allows us to study phenomena that are impossible to study experimentally or observationally. A field that is heavily studied computationally is general relativity. In numerical relativity, computational methods are used to solve Einstein's equations and to study astrophysical phenomena that otherwise could not be studied directly. In this work, we will apply numerical relativity to explore conditions that may have been present during the very early universe, a time we are unable to observe directly.

In this thesis, we will use a combination of numerical relativity and cosmology to study binary black holes inside cosmological environments. Though these simulations are fine-tuned and therefore unlikely to be observed, they represent an interesting class of computational problems. We will couple a real-valued scalar field, similar to a field that may have powered inflation, with gravity using Einstein's equations. The effect of the scalar field on the binary black hole system is studied; differences in mass accretion, merger trajectories, and characteristic gravitational waveforms will be presented.

We begin by describing the physical characteristics of an inflationary phase transition in the early times of the universe. Then, we continue with a brief overview of scalar fields and general relativity before decomposing Einstein's equations into a form suitable for numerical analysis. A description of the scientific code used in this thesis is detailed in Chapter V, followed by an analysis of our simulations in Chapter VI.

CHAPTER II

PHASE TRANSITIONS IN THE EARLY UNIVERSE

It is likely the Universe underwent phase transitions as it evolved after the Big Bang [20]. Through these phase transitions, gauge symmetries were broken and then restored [13]. Problems with the standard Hot Big Bang model led to the theory of inflation, a period in which the Universe expanded exponentially and rapidly. In this section, we will discuss inflationary phase transitions. These phase transitions were powered by a scalar field and completed by the nucleation of scalar field bubbles. At the end of such a transition, the universe has moved from a period of exponential expansion to an isotropic homogeneous state [20].

2.1 Inflation

2.1.1 The Horizon and Flatness Problems

An inflationary universe was first posited in 1981 as a solution to the horizon and flatness problems [8]. The horizon and flatness problems are issues with the standard model's initial conditions; the standard model assumed the universe to the be homogeneous, isotropic, and comprised of massless particles in thermal equilibrium. The standard model also assumes the expansion of the universe is adiabatic. [8]

Though the universe is assumed to be homogeneous, it contains a large number of regions that are causally disconnected [8], but these regions have temperatures that are very nearly the same [14]. How this homogeneity is possible without the regions being causally connected is known as the horizon problem.

To understand the flatness problem, we begin by considering the energy density of the universe, ρ. The current energy density of the universe is close to a critical value ρ_{cr}, which corresponds to the boundary between an open and closed universe

[8]. Then, the density parameter, Ω, is defined to be:

$$\Omega \equiv \frac{\rho}{\rho_{cr}}, \tag{2.1}$$

which may also be written in the following form [1]:

$$\Omega = \frac{8\pi G\rho}{3H^2}, \tag{2.2}$$

where H is the Hubble constant. At the present time, the density parameter, Ω_0, has been measured to be close to unity. However, Guth assumes a less strict range [8]:

$$0.01 < \Omega_0 < 10. \tag{2.3}$$

The present value of the Hubble constant is H_0, and together with Ω_0, describes our current universe [13]. These parameters determine the radius of curvature of the universe, R_c and the density as follows:

$$R_c^2 = \left(H_0^2|\Omega_0 - 1|\right)^{-1}, \tag{2.4}$$

$$\rho_0 = \frac{3H_0^2}{8\pi G}\Omega_0. \tag{2.5}$$

As shown in Equation 2.3, Ω_0 is close to unity; this implies [13]

$$R_c \approx H_0^{-1}, \tag{2.6}$$

$$\rho_0 \approx \rho_{cr}. \tag{2.7}$$

The density parameter is not constant and evolves with time:

$$\Omega(t) = \left[1 - x(t)\right]^{-1}, \tag{2.8}$$

where $x(t)$ depends upon the epoch the universe is currently occupying.We represent the point in time that matter and radiation energy densities were equal as t_{eq}. Before

[1] In our geometric units, $G = 1$, but the term has been included in this section for completeness.

t_{eq}, the universe was radiation dominated; after t_{eq}, it was matter dominated. During these times, $x(t)$ evolved as:

$$x(t) \propto \begin{cases} a(t)^2, & \text{for } t \leq t_{eq} \\ a(t), & \text{for } t > t_{eq} \end{cases}$$

where $a(t)$ is the scale factor. The scale factor describes the rate of expansion of the universe. Due to the $(1 - x(t))^{-1}$ evolution of Ω, the density parameter must have been very close to unity in the past. For example, at $t = 10^{-43}s$ (during the Planck epoch)[13]

$$|\Omega(t) - 1| \lesssim \mathcal{O}(10^{-60}), \tag{2.9}$$

and the curvature would be

$$R_c(t) \gtrsim \mathcal{O}(10^{30})\ H. \tag{2.10}$$

A final condition at t is:

$$\frac{|k/R^2|}{8\pi G\rho/3} \lesssim \mathcal{O}(10^{-60}). \tag{2.11}$$

These initial conditions would need to be very precise at the Planck epoch. If the constraints in Equations 9, 10, and 11 were fulfilled, for an open universe ($k < 0$), our universe would have cooled to its current temperature in $10^{-11}s$. For a closed universe ($k > 0$), the universe would have collapsed in only a few Planck times. Therefore, extremely fine tuning of these parameters is necessary for our universe to have achieved its current state [8]. The puzzle of these precise initial conditions is known as the flatness problem.

2.1.2 The Inflationary Epoch

A period of rapid inflation during the early universe can be shown to eliminate both the horizon and flatness problems. This period of inflation can be characterized using the comoving Hubble length, H^{-1}/a. During inflation:

$$\frac{d}{dt}\frac{H^{-1}}{a} < 0. \tag{2.12}$$

The comoving Hubble length is an important scale of the Universe as it expands. As shown in Equation 2.12, the comoving Hubble length is decreasing with time. During inflation, the observable Universe shrinks as this characteristic scale is smaller. [14]

During inflation, the density parameter evolves towards 1, and will be very nearly unity by the time inflation ends. This solves the flatness problem by providing a mechanism for the density parameter to be not unity during the early times of the Universe, while still being very close to 1 now.

In the next section, we will describe to the mechanism by which inflation is believed to have occurred : a scalar field.

2.2 The Scalar Field and Inflation

2.2.1 Symmetry Breaking and Restoration

We begin with the breaking and restoring of gauge symmetries. A simple model is given by introducing a real-valued scalar field. Consider a real scalar field described by its Lagrangian [13]:

$$\mathcal{L} = \frac{1}{2}\partial_\mu\phi\partial^\mu\phi - V(\phi) \tag{2.13}$$

where $V(\phi)$ is a potential of the form,

$$V(\phi) = \frac{-1}{2}m^2\phi^2 + \frac{1}{4}\lambda\phi^4. \tag{2.14}$$

This Lagrangian possesses symmetry under the transformation $\phi \to -\phi$. The associated potential is a fourth-order polynomial and has two minima. Then the vacuum expectation value of the scalar field occurs at one of these two minima:

$$\langle\phi_1\rangle = \sqrt{\frac{m^2}{\lambda}} \tag{2.15}$$

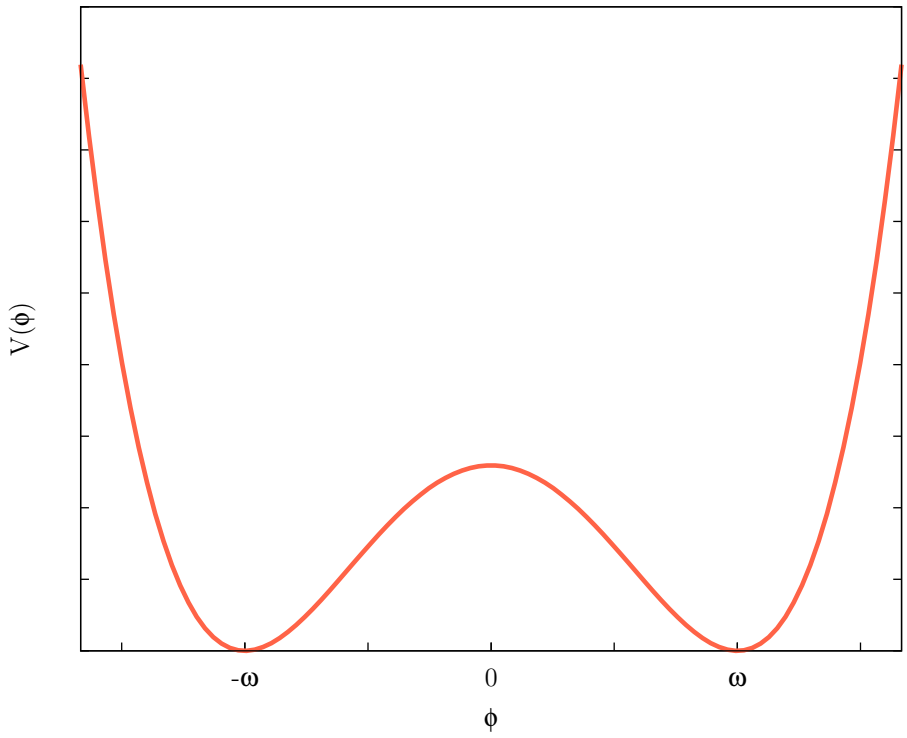

Figure 1: An inflationary potential, $V(\phi)$ with minima at $\pm\omega$.

or

$$\langle\phi_2\rangle = -\sqrt{\frac{m^2}{\lambda}}. \tag{2.16}$$

Adding a constant term, $m^4/4\lambda$ to the Lagrangian will preserve the equations of motion, but will allow the potential to be written as:

$$V(\phi) = \frac{\lambda}{4}\left(\phi^2 - \omega^2\right)^2, \tag{2.17}$$

which will allow us to write the minima more simply as

$$\phi_1 = -\omega \tag{2.18}$$

$$\phi_2 = \omega. \tag{2.19}$$

One of the minima corresponds to the symmetric phase and one is in the broken symmetry phase [10]. The difference between these two potentials is [10]:

$$V(\phi_1) - V(\phi_2) = \epsilon^4, \tag{2.20}$$

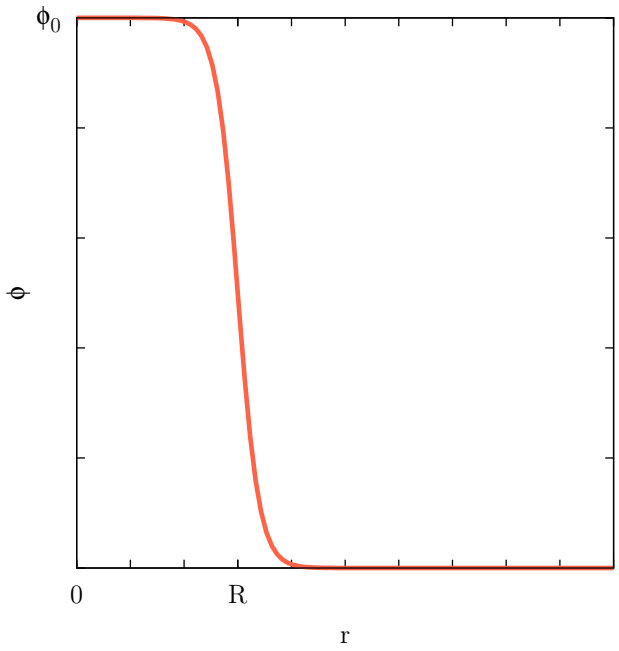

Figure 2: A scalar field profile of a thin-walled bubble, where R is the bubble radius, as defined in Equation 2.22.

where ϵ has units of energy. Then, there is some potential barrier between the two minima which is much greater than ϵ^4. This barrier is passed through via quantum tunneling [13]. After the phase transition completes, the total energy density is:

$$\rho = \frac{\pi^2}{30} g(T) T^4 + \epsilon^4 \tag{2.21}$$

where $g(T)$ depends on the number of degrees of freedom of fermions and bosons.

2.3 Cosmological Bubbles and Dynamics of Inflation

The nucleation of vacuum bubbles is the mechanism by which a first-order phase transition proceeds[10, 20]. The universe moves from the true vacuum symmetric state $\phi = 0$ to a lower temperature, broken symmetry state at $\phi = \omega$ via quantum tunnelling through the barrier. Quantum tunnelling occurs as bubbles are nucleated in the $\phi = \omega$ phase (which is energetically favorable) and expand at the speed of light [13]. The bubbles investigated in this thesis are constrained by the thin-wall limit: the transition between the scalar field value inside the bubble and the value

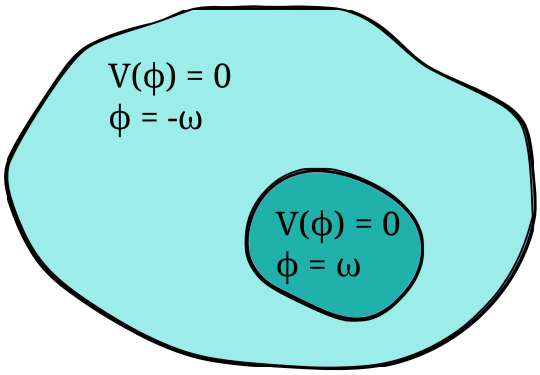

Figure 3: A diagram of a universe with two distinct regions of scalar field, one in each of the scalar field potential minima.

outisde the bubble occurs over a small interval which is much less than the radius of the bubble, R [13]. The scalar field profile of such a bubble is given by:

$$\phi_{TW}(r) = \frac{1}{2}\phi_0 \left[1 - \tanh\left(\frac{r-R}{\sigma}\right)\right], \tag{2.22}$$

where σ is the thickness of the bubble wall and ϕ_0 is the scalar field value inside the bubble. This profile is shown in Figure 2.

2.3.1 Collapse of Cosmological Bubbles

Massless, spherically symmetric scalar fields have been shown numerically to exhibit critcal behavior as they collapse [7], creating black holes. This critical behavior is due to two dyanmical characterisitcs of the scalar field; the field has kinetic energy, which will cause the field to disperse. Additionally, the scalar field has gravitational potential energy, which can cause some of the field's mass-energy to be trapped in a black hole [5].

The collapse of spherically summetric bubbles has been presented as a mechanism by which primordial black holes may have formed during the early universe [9]. The formation and subsequent evaporation of these primordial black holes may provide a mechanism by which the universe reheated during a phase transition [9].

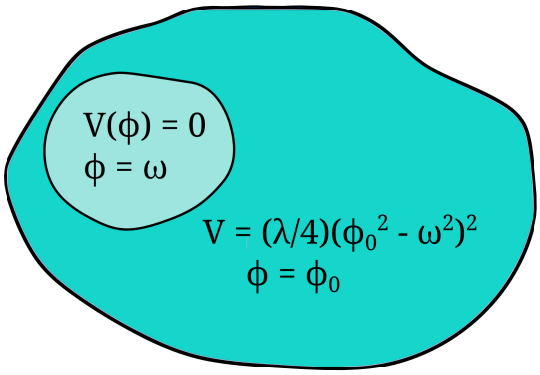

Figure 4: A diagram of a universe with two distinct regions of scalar field, one in a local minima, ω, and one at a non-zero value ϕ_0.

2.3.2 Dynamics of Inflation

In Figure 1, we showed an example potential with minima at $\pm\omega$. In this section, we will discuss in detail the dynamics possible in such a potential. Suppose there are two distinct regions in the universe. Each have a potential of 0 ($V = 0$) with one region at a scalar field value of ω and one at the other minima, $-\omega$. In this scenario, a wall forms between the two regions due to the barrier in potential between the two regions. To move from one region to the other, quantum tunnelling must take place. This universe is illustrated Figure 3.

2.3.2.1 Slow-Roll Inflation

First, we assume that a first-order phase transition with spontaneous symmetry breaking occurs. The threshold at which grand unifaction occurs is $T_G \approx 10^{14}$ GeV [15]. For temperatures larger than T_G, a minimum occurs in the potential for $\phi = 0$ [13]. At this time, symmetry is restored. During the phase transition, another minimum occurs as the temperatures approach the critical value at $\langle\phi\rangle = T_G$. Once the temperatures cool and reach the critical value, the minima are degenerate and symmetry is broken [13].

Consider a universe where a region is in a minima, ω, and another has a scalar field value of ϕ_0, where ϕ_0 is non-zero and located in the interval between the two

minima. The potential in this region is

$$V(\phi_0) = \frac{\lambda}{4}\left(\phi_0^2 - \omega^2\right)^2.$$

This universe is illustraed in Figure 4. In this scenario, the scalar field will "roll" down to the next minima while the region expands outward. This process is called "slow-roll inflation."

The equation of motion for the scalar field in slow-roll inflation is given by [13]

$$\ddot{\phi} + 3H\dot{\phi} + V'(\phi) = 0, \tag{2.23}$$

where the Friedmann equation gives H as [18]

$$H^2 = \frac{1}{3\bar{m}_P^2}\left(\frac{1}{2}\dot{\phi}^2 + V(\phi)\right), \tag{2.24}$$

where the reduced Planck scale, $\bar{m}_P$, is approximately 10^{18} GeV.

CHAPTER III

SCALAR FIELDS IN GENERAL RELATIVITY

In this chapter, we will give a brief overview of general relativity and Einstein's equations and then describe how scalar fields are inserted into non-flat spacetimes.

3.1 General Relativity

In this thesis, we will use geometric units; in this scheme, the gravitational constant and the speed of light are both unity ($G = c = 1$). The metric signature will be the standard $(-, +, +, +)$. First, define the metric tensor, $g_{\mu\nu}$ using the distance between two points in spacetime, ds^2, [5]:

$$ds^2 = g_{\mu\nu} dx^\mu dx^\nu. \tag{3.1}$$

The metric tensor will be used to raise and lower indices of other tensors.

3.1.1 The Riemann Curvature Tensor

We begin by introducing quantities necessary to describing the Einstein field equation. First, we introduce the Christoffel symbol,

$$\Gamma^\lambda_{\mu\nu} = \frac{1}{2} g^{\lambda\sigma} \left(\partial_\mu g_{\nu\sigma} + \partial_\nu g_{\sigma\mu} - \partial_\sigma g_{\mu\nu} \right), \tag{3.2}$$

where $\partial_\mu \equiv \partial/\partial x^\mu$. The Christoffel symbol is used to define a covariant derivative, which is a general partial derivative:

$$\nabla_\mu V^\nu = \partial_\mu V^\nu + \Gamma^\nu_{\mu\sigma} V^\sigma. \tag{3.3}$$

The Riemann curvature tensor measures the curvature of spacetime. It is defined using the Christoffel symbol:

$$R^\rho_{\sigma\mu\nu} = \partial_\mu \Gamma^\rho_{\nu\sigma} - \partial_\nu \Gamma^\rho_{\mu\sigma} + \Gamma^\rho_{\lambda\mu} \Gamma^\lambda_{\sigma\nu} - \Gamma^\rho_{\lambda\nu} \Gamma^\lambda_{\sigma\mu}. \tag{3.4}$$

The Ricci tensor is obtained by contracting the Riemann tensor [18]:

$$R_{\mu\nu} = R^{\lambda}_{\mu\lambda\nu}. \tag{3.5}$$

The trace of the Ricci tensor is the Ricci scalar:

$$R = g^{\mu\nu} R_{\mu\nu} \tag{3.6}$$

3.1.2 Einstein's Equations

Now that we have defined the metric, the Ricci scalar, and the Ricci tensor, we can write out the Einstein field equations in full:

$$G_{\mu\nu} = 8\pi T_{\mu\nu}, \tag{3.7}$$

where G is the Einstein tensor,

$$G_{\mu\nu} = R_{\mu\nu} - \frac{1}{2} g_{\mu\nu} R, \tag{3.8}$$

and $T_{\mu\nu}$ is the stress-energy tensor. The stress-energy tensor is the contribution of energy from all nongravitational sources, e.g. particles, gases, or scalar fields [5].

3.1.3 The Weyl Tensor

The trace-free portion of the Riemann tensor is the Weyl conformal tensor. In four dimensions, the Weyl tensor is given by [5]:

$$\begin{aligned} C_{\rho\sigma\mu\nu} &= R_{\rho\sigma\mu\nu} - \mathrm{tr}[R_{\rho\sigma\mu\nu}] \\ &= R_{\rho\sigma\mu\nu} - \frac{1}{2}\left(g_{\rho\mu}R_{\sigma\nu} - g_{\rho\nu}R_{\sigma\mu} - g_{\sigma\mu}R_{\rho\nu} + g_{\sigma\nu}R_{\rho\mu}\right) + \frac{1}{6}\left(g_{\rho\mu}g_{\sigma\nu} - g_{\rho\nu}g_{\sigma\mu}\right) R. \end{aligned} \tag{3.9}$$

A more detailed treatment of the Weyl tensor will be shown in Section 4.3 as it relates to numerical extraction of gravitational waves.

3.2 The Klein-Gordon Equation

For a system including a real scalar field, the stress-energy tensor is [5]:

$$T_{\mu\nu} = \nabla_\mu \phi \nabla_\nu \phi - \frac{1}{2} g_{\mu\nu} g^{\alpha\beta} \nabla_\alpha \nabla_\beta \phi - g_{\mu\nu} V(\phi). \tag{3.10}$$

The potential, $V(\phi)$ can be written as:

$$V(\phi) = \frac{1}{2} m^2 \phi^2 + V_{int}, \tag{3.11}$$

where V_{int} is the interaction potential [5]. If the field interacts only with gravitation, this quantity is zero.

The equation of motion for this field is [12]:

$$\Box \phi = \frac{1}{\sqrt{-g}} \partial_\mu \left(\sqrt{-g} g^{\mu\nu} \partial_\nu \phi \right) = \partial_\phi V \tag{3.12}$$

Equation 3.12 leads to the Klein-Gordon equation

$$\nabla_\mu \nabla^\mu \phi - m^2 \phi - \frac{dV_{int}}{d\phi} = 0, \tag{3.13}$$

which, for a massless non-interacting scalar field becomes:

$$\nabla_\mu \nabla^\mu \phi = 0. \tag{3.14}$$

Equation 3.14 will be cast into first-order form for ease of numerical integration in Section 4.4.

CHAPTER IV

NUMERICAL RELATIVITY

4.1 3+1 Decomposition

To evolve a system that is governed by Einstein's field equations, the metric tensor, $g_{\mu\nu}$, and its time derivative, $\partial_t g_{\mu\nu}$, must be determined at an initial time t. Then, future values of these quantities can be determined at a time $t + \delta t$ by integrating forward in time. This is repeated so the metric is calculated for every other point, x^i, in spacetime. [5]

Let M represent the spacetime manifold upon which we will evolve Einstein's equations, with its metric $g_{\mu\nu}$. Then, the spacetime (M, $g_{\mu\nu}$) can be foliated into spacelike surfaces, Σ_t, which do not intersect; they are level surfaces of a global scalar time function, t. On the surface slice, Σ_t, define a closed one-form [5]

$$\Omega_\mu = \nabla_\mu t, \tag{4.1}$$

where ∇_μ is the covariant derivative. The norm of Ω_μ can be determined using the metric:

$$||\Omega||^2 = g^{\mu\nu}\nabla_\mu t \nabla_\nu t = -\frac{1}{\alpha^2}, \tag{4.2}$$

where α is the lapse scalar. This represents the "lapse" in proper time (represented by τ) between two hypersurfaces as shown below: [1]

$$d\tau = \alpha(t, x^\mu). \tag{4.3}$$

The normalized one-form is then

$$\omega_\mu = \alpha\Omega_\mu. \tag{4.4}$$

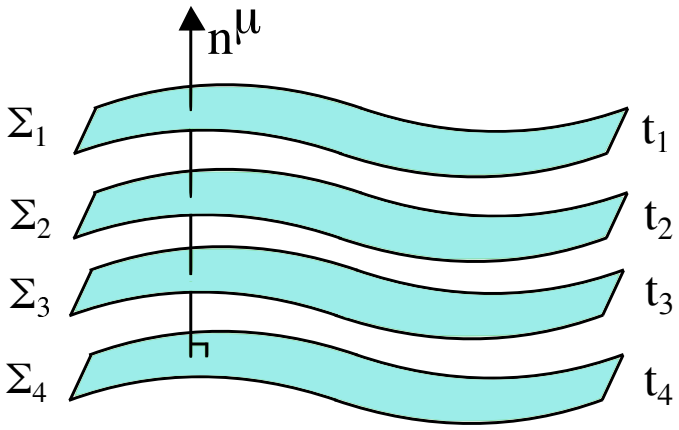

Figure 5: A manifold, M, foliated into four hypersurfaces, Σ_1, Σ_2, Σ_3, and Σ_4 with the unit normal vector, n^μ shown.

These equations can now be used to define a unit vector normal to the set of spatial slices,

$$n^\mu = -g^{\mu\nu}\omega_\nu. \tag{4.5}$$

This timelike vector has been defined so that it points in the direction of increasing t. The foliation described above and this normal vector are illustrated in Figure 5.

Then, the metric on the hypersurface that is generated by the overall metric, $g_{\mu\nu}$, is [5]

$$\gamma_{\mu\nu} = g_{\mu\nu} + n_\alpha n_\beta. \tag{4.6}$$

Similar to Equation 3.1, the distance between two points on the surface, Σ_t, can be defined using the spatial components of this induced metric as follows [1]

$$ds^2_\Sigma = \gamma_{ij} dx^i dx^j. \tag{4.7}$$

Another important quantity to define is the "shift vector", β^i, which is a purely spatial 3-vector. Using the previous defined quantities for the lapse function, the shift function, and the spatial metric, the line element can be written as:

$$ds^2 = (-\alpha^2 + \beta_i\beta^i)dt^2 + 2\beta_i dt dx^i + \gamma_{ij} dx^i dx^j. \tag{4.8}$$

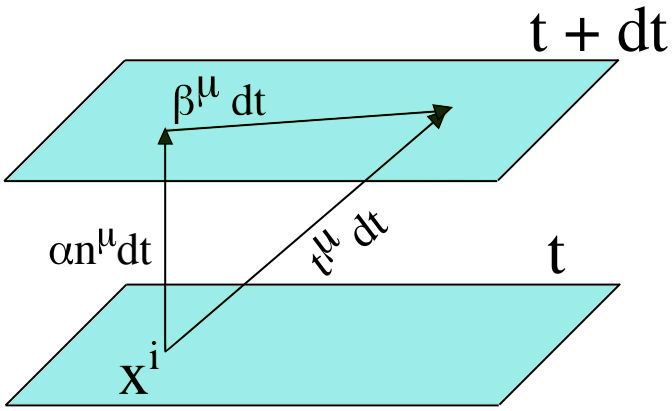

Figure 6: Two surfaces separated by a small time, dt. Shown is the lapse scalar and the shift vector.

Now, the metric on the spactime can be written explicity using the defined functions. With lowered indices,

$$g_{\mu\nu} = \begin{pmatrix} -\alpha^2 + \beta_k\beta^k & \beta_i \\ \beta_j & \gamma_{ij} \end{pmatrix}. \tag{4.9}$$

With raised indices, the metric can be written as:

$$g^{\mu\nu} = \begin{pmatrix} \frac{-1}{\alpha^2} & \frac{\beta^i}{\alpha^2} \\ \frac{\beta^j}{\alpha^2} & \gamma^{ij} - \frac{\beta^i\beta^j}{\alpha^2} \end{pmatrix}. \tag{4.10}$$

4.1.1 Curvature

There are two types of curvature in this formalism: the intrinsic curvature, which is defined by the surfaces spatial metric, γ_{ij}, and the extrinsic curvature, which is derived from how the hypersurfaces are embedded in spacetime [1]. First, we define a projection operator, P^μ_ν using the spatial metric:

$$P^\mu_\nu = g^\mu{}_\nu + n^\mu n_\nu = \delta^\mu{}_\nu + n^\mu n_\nu, \tag{4.11}$$

where $\delta^\mu{}_\nu$ is the Kronecker delta.

Then, the extrinsic curvature is defined to be [1]

$$K_{\mu\nu} = -P\nabla_\mu n_\nu = -(\nabla_\mu n_\nu + n_\mu n^\gamma \nabla_\gamma n_\beta). \tag{4.12}$$

The extrinsic curvature is symmetric and purely spatial [5]; for this reason, only the spatial components, K_{ij}, need to be considered. The curvature can also be written in terms of the spatial metric γ_{ij} :

$$K_{ij} = \frac{1}{2\alpha}\left(-\partial_t \gamma_{ij} + D_i\beta_j + D_j\beta_i\right), \tag{4.13}$$

where D is the spatial gradient (or the three-dimensional covariant derivative) [1].

Later, we will see it is useful to separate the extrinsic curvature into its trace,

$$trK = \gamma^{ij}K_{ij} \tag{4.14}$$

and the trace free portion, A_{ij}. The trace free part is defined to be:

$$A_{ij} \equiv K_{ij} - \frac{1}{3}\gamma_{ij}trK. \tag{4.15}$$

4.1.2 The ADM Equations

The hypersurfaces have a characteristic 3-dimensional Riemann tensor, $R^{\alpha}_{\beta\gamma\epsilon}$, which is related to the 4-dimensional Riemann tensor of the overall manifold, M. This will be done by projecting the 4-dimensional tensor spatially, then two more projections with first one index in the normal direction and the second with two indices in the normal direction [5]. The Einstein equations can be written using three types of projections; the first is a normal projection [1],

$$n^{\mu}n^{\nu}\left(G_{\mu\nu} - 8\pi T_{\mu\nu}\right) = 0. \tag{4.16}$$

The energy density of matter is given by:

$$\rho = n_{\mu}n_{\nu}T_{\mu\nu}. \tag{4.17}$$

The Ricci scalar associated with the 3-metric, R, can be used with the trace of the curavture, the energy density, and Equation 4.16 to find the following:

$$R + (trK)^2 - K_{ij}K^{ij} = 16\pi\rho. \tag{4.18}$$

Equation 4.18 is the Hamiltonian constraint.

The second group of Einstein equations is from mixed projections; this uses the previously defined projection operator P and gives the following equation,

$$P\left[n^{\mu}\left(G_{\mu\nu}-8\pi T_{\mu\nu}\right)\right]=0. \tag{4.19}$$

From this projection, the momentum constraint can be derived [1]; this constraint is defined below:

$$D_j\left[K^{ij}-\gamma^{ij}trK\right]=8\pi j^i. \tag{4.20}$$

The quantity, j^i is the momentum flux of matter:

$$j^i=P^i_{\beta}\left(n_{\mu}T^{\mu\nu}\right). \tag{4.21}$$

The final set of equations is generated by projecting onto the hypersurface and contains 6 equations:

$$P\left(G_{\mu\nu}-8\pi T_{\mu\nu}\right)=0. \tag{4.22}$$

The six equations derived from the hypersurface projection take the following form, [1]:

$$\begin{aligned}\partial_t K_{ij}&=\beta^a\partial_a K_{ij}+K_{ia}\partial_j\beta^a+K_{ja}\partial_i\beta^a-D_iD_j\alpha\\&\quad+\alpha\left[R_{ij}-2K_{ia}K^a_j+K_{ij}trK\right]+4\pi\alpha\left[\gamma_{ij}(trS-\rho)-2S_ij\right],\end{aligned} \tag{4.23}$$

where

$$S_{ij}=PT_{ij} \tag{4.24}$$

is the matter stress tensor.

Equation 4.23 is the evolution equation for the extrinsic curvature. The evolution equation for the spatial metric can be found by rearranging Equation 4.13:

$$\partial_t\gamma_{ij}=-2\alpha K_{ij}+D_i\beta_j+D_j\beta_i. \tag{4.25}$$

The evolution equations for the spatial metric and the curvature, together with the Hamiltonian and momentum constraints, are known as the Arnowitt-Deser-Misner (ADM) equations.

4.2 The BSSN Formalism

A more numerically stable 3+1 decomposition is found in the BSSN formalism. First, the spatial metric γ_{ij} is rewritten as:

$$\gamma_{ij} = \psi^4 \tilde{\gamma}_{ij}, \tag{4.26}$$

where $\tilde{\gamma}_{ij}$ is the conformal metric and ψ is the conformal factor [1].The conformal factor is chosen to have the following characteristics [1]

$$\psi = \gamma^{1/12}, \tag{4.27}$$

$$\tilde{\gamma}_{ij} = \psi^{-4}\gamma_{ij} = \gamma^{\frac{1}{3}}\gamma_{ij}, \tag{4.28}$$

$$\tilde{\gamma} = 1, \tag{4.29}$$

where γ and $\tilde{\gamma}$ are the determinants of γ_{ij} and $\tilde{\gamma}_{ij}$ respectively. The BSSN formalism also introduces the following variables:

$$\zeta = \ln \psi = \frac{1}{12} \ln \gamma \tag{4.30}$$

$$K = \gamma_{ij} K^{ij} \tag{4.31}$$

$$\tilde{\gamma}_{ij} = e^{-4\zeta}\gamma_{ij} \tag{4.32}$$

$$\tilde{A}_{ij} = e^{-4\zeta} A_{ij} \tag{4.33}$$

where A_{ij} was defined in Equation 4.15. Generally, the BSSN formalism uses the variable ϕ for the conformal factor (Equation 47), but this has been replaced with ζ to avoid confusion with the variable ϕ used in the scalar field equations. Using Equation 4.13, we can obtain evolution equations for the conformal spatial metric and the conformal factor. The partial time derivative of the conformal spatial derivative is given by

$$\partial_t \tilde{\gamma}_{ij} = -2\alpha \tilde{A}_{ij}. \tag{4.34}$$

For the conformal factor,

$$\partial_t \zeta = -\frac{1}{6}\alpha K. \tag{4.35}$$

Using Equation 4.23, the following equations are obtained:

$$\partial_t K = -D_i D^i \alpha + \alpha \left(\tilde{A}_{ij} \tilde{A}^{ij} + \frac{1}{3} K^2 \right) \tag{4.36}$$

$$\partial_t \tilde{A}_{ij} = e^{-4\zeta} \left[-D_i D_j \alpha + \alpha R_{ij} \right]^{TF} + \alpha \left(K \tilde{A}_{ij} - 2 \tilde{A}_{ik} \tilde{A}^k_j \right), \tag{4.37}$$

where the TF superscript refers to the trace-free part of the bracketed quantity. Finally, an evolution equation should be obtained for the conformal connection functions, $\tilde{\Gamma}^i$,

$$\tilde{\Gamma^i} = \tilde{\gamma}^{jk} \tilde{\Gamma}^i_{jk} = \partial_j \tilde{\gamma}^{ij}, \tag{4.38}$$

where the Christoffel symbols of the conformal metric are $\tilde{\Gamma}^i_{jk}$. The corresponding evolution equation is given by:

$$\partial_t \tilde{\Gamma}^i = -2 \tilde{A}^{ij} \partial_j \alpha + 2\alpha \left(\tilde{\Gamma}^i_{jk} \tilde{A}^{jk} + 6 \tilde{A}^{ij} \partial_j \zeta - \frac{2}{3} \tilde{\gamma}^{ij} \partial_j K \right). \tag{4.39}$$

These evolution equations compose the BSSN formalism.

4.3 Gravitational Waves

4.3.1 Perturbation Theory

We begin our discussion our gravitational waves with a small perturbation, $h_{\mu\nu}$, of a "background solution to Einstein's equation which is a nearly flat (Minkowski) spacetime. With this perturbation, the metric is:

$$g_{\mu\nu} = \eta_{\mu\nu} + h_{\mu\nu}. \tag{4.40}$$

Then, a "transverse-traceless" gauge is imposed so that the time components of $h_{\mu\nu}$ are zero and the perturbation is purely spatial. This purely spatial perturbation can now be written using Latin indices, i and j. The four-dimensional Riemann tensor, Equation 3.4, can be rewritten using the perturbation [5]:

$$R_{i0j0} = -\frac{1}{2} \ddot{h}^{TT}_{ij}, \tag{4.41}$$

where the superscript TT corresponds to the transverse-traceless gauge, and $\ddot{h}$ is the second time derivative. The gauge conditions constrain eight of the ten components of the perturbation. The final two free components are the possible polarizations of the gravitational wave. A gravitational wave can then be expressed using the polarization tensors, $e^{+}_{\mu\nu}$ and $e^{\times}_{\mu\nu}$, and two dimensionless amplitudes, h_{+} and $h_{\times}$. This expression is:

$$h^{TT}_{jk} = h_{+}e^{+}_{ij} + h_{\times}e^{\times}_{ij}. \tag{4.42}$$

4.3.2 The Newman-Penrose Formalism

The Weyl tensor, Equation 3.9, has ten independent components; these components can be described by five complex scalars, called Weyl scalars and represented by ψ. These scalars are produced by contracting the Weyl tensor using a group of four vectors called a tetrad [16]. We describe this tetrad beginning with two real, orthogonal space-like vectors, a_μ and b_μ, which define a complex null vector

$$m_\mu = \frac{1}{\sqrt{2}}\left(a_\mu - ib_\mu\right). \tag{4.43}$$

In addition, three more null vectors are introduced: two real vectors, l_μ and n_μ, and another complex vector, m^*_μ that is the complex conjugate of m_μ. Then, using this tetrad, the Weyl scalar ψ_4 is:

$$\psi_4 = -C_{\mu\nu\sigma\rho}n^\mu m^*_\nu n^\sigma m^*_\rho, \tag{4.44}$$

where $C_{\mu\nu\sigma\rho}$ is the previously defined Weyl tensor. This contraction can also be applied to the Riemann tensor. It can be shown that this contraction results in [5]

$$R_{\mu\nu\sigma\rho} = \frac{1}{2}\left(\partial_\mu\partial_\rho h_{\nu\sigma} + \partial_\nu\partial_\sigma h_{\mu\rho} - \partial_\nu\partial_\rho h_{\mu\sigma} - \partial_\mu\partial_\sigma h_{\nu\rho}\right). \tag{4.45}$$

At a large radius and for an outgoing wave, ψ_4 can be written as:

$$\psi_4 = \ddot{h}_{+} - i\ddot{h}_{\times}. \tag{4.46}$$

This can then be decomposed using spin-weighted spherical harmonics where $s = -2$:

$$\psi_4(t, r, \theta, \phi) = \sum_{l=2}^{\infty} \sum_{m=-l}^{l} \psi_4^{lm}(t, r)_{-2}Y_{lm}(\theta, \phi), \tag{4.47}$$

where the expansion coefficients are computed from

$$\psi_4^{lm} = \int d\Sigma_{-2}Y_{lm}^* \psi_4. \tag{4.48}$$

In order to compute the Weyl scalar in 3+1 formalism, the four-dimensional Riemann tensor must be constructed from only spatial components. In an asymptotically flat spacetime, the Riemann tensor can be calculated using the extrinsic curvature, K, and the Christoffel symbol. These can then be used to calculate ψ_4 on every time slice in the simulation. [5]

In this work, the modes (Equation 4.48) are computed and ψ_4 is reconstructed. This leads to the most accurate results for the dominant modes [5].

4.4 Scalar Field Evolution

Finally, we will describe the evolution equations for the scalar field. In order to integrate the Klein-Gordon equation (3.14), the following variables are introduced [5, 12]

$$\Pi = \frac{-1}{\alpha} \left(\partial_t \phi - \beta^i \partial_i \phi \right), \tag{4.49}$$

$$\Phi_i = \partial_i \phi. \tag{4.50}$$

Then, the evolution equations for the scalar field are given by:

$$\partial_t \phi = \beta^i \partial_i \phi - \alpha \Pi, \tag{4.51}$$

$$\partial_t \Pi = \beta^i \partial_i \Pi - \alpha g^{ij} \partial_j \Phi_i + \alpha g^{ij} \Gamma_{ij}^k \Phi_k - g^{ij} \Phi_j \partial_i \alpha + \alpha K \Pi, \tag{4.52}$$

$$\partial_t \Phi_i = \beta^j \partial_j \Phi_i + \Phi_j \partial_i \beta^j - \alpha \partial_i \Pi - \Pi \partial_i \alpha. \tag{4.53}$$

CHAPTER V

COMPUTATIONAL METHODS

Now that we have described the physics that govern our evolutions of spacetime, we can begin describing the programming framework used to complete our simulations. These simulations were performed using *Maya*, a numerical relativity code developed at Georgia Tech. *Maya* uses *Cactus*, an open-source environment developed for scientific simulations. The main components of the code are *Cactus, Carpet* (an implementation of adaptive mesh refinement), *Kranc*, the Einstein Toolkit and *Maya*. Each of these is discussed in detail below.

5.1 Cactus

Cactus implements a modular structure as follows: a central core ("flesh") that connects to modular components (called "thorns"). These thorns can perform a wide variety of tasks; for example, there are thorns for extracting gravitational waves, performing hydrodynamics, handling parallelism, and dealing with input and output. Two thorns of special interest are *Carpet*, *Cactus'* implementation of an adaptive grid and Kranc, a code generation scheme. [2] Cactus contains code written in C/C++ and Fortran.

5.1.1 Time Integration

The partial differential equations described in the BSSN formalism must be numerically integrated. For this, we used the Method of Lines (MoL) thorn in *Cactus*; this implementation discretizes the spatial derivatives appearing in the BSSN equations. [21] This discretization converts the system of partial differential equations into a system of ordinary differential equations, which can then be more easily evaluated.

After applying MoL, the system of ordinary differential equations is solved using the Runge-Kutta method.

For stability, we apply the Courant-Friedrichs-Lewy condition to the Courant factor, C:

$$C = \frac{|v|\Delta t}{\Delta x} \leq 1, \tag{5.1}$$

where Δx is the grid spacing, Δt is the integration timestep, and v is the speed of propogation [17]. The speed of propogation in our scheme is the speed of light which is equal to unity in geometric units. Additionally, our integration scheme requires a lower Courant factor. The CFL condition is then:

$$C = \frac{\Delta t}{\Delta x} \leq \frac{1}{2} \tag{5.2}$$

5.2 Carpet and Adaptive Mesh Refinement

Carpet is a thorn included in the *Cactus* framework which is used for adaptive mesh refinement. Adaptive mesh refinement is a technique used to conserve computational resources; in many astrophysical simulations, the phenomena of interest is in a small portion of the full domain. Outside of these subsets, a coarser mesh is needed since less accuracy is needed. For example, the areas around the black holes may have a fine, high-resolution mesh, while areas far away can be performed at low resolution. Since gravitational wave extraction should be performed at large radii, it is necessary to have large domains. It has been shown that only a low resolution is necessary to maintain accuracy of waves travelling from fine to coarse grids [19].

Following the Berger-Oliger approach [6], *Carpet* decomposes the domain into sets of rectangular grids [19]. More precisely, the grids are decomposed onto a Cartesian topology with each rectangular grid boundary aligning with the Cartesian grid line.

These grids are then grouped into refinement levels, L^k. On the k^{th} refinement level, the grid spacing is Δx^k. An example is shown in Figure 7.

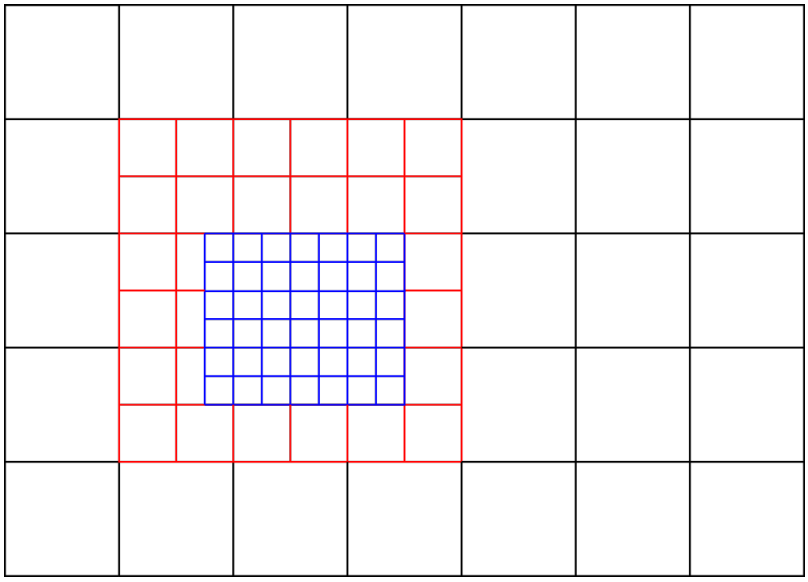

Figure 7: An example of adaptive mesh refinement with three different rectangular nested grids.

Additionally, the rectangular grids centered on the black holes will track the singularities as they move through the domain, ensuring accuracy while still conserving computational resources.

5.3 Kranc Code Generation

Another useful thorn integrated in *Cactus* is *Kranc*. Kranc is Mathematica-based package that converts tensorial partial differential equations into parallel code in C [11]. The tensorial expressions are expanded into components; then, the numerical code that results in an optimized arithmetic code. Discretization is again done using the Method of Lines, then the ODEs are integrated with Runge-Kutta [11]. Kranc is used in the BSSN solver and for solving the evolution equations of the scalar field.

5.4 Maya and the Einstein Toolkit

The Einstein toolkit is an open-source numerical relativity codebase that is based on *Cactus* [21]. Many of the thorns used in this thesis were developed in the Einstein toolkit. Additionally, Georgia Tech-developed thorns (*Maya*) were used for initalizing

and evolving the scalar field.

CHAPTER VI

RESULTS

Two sets of simulations were run: the first contained only cosmological bubbles with no black holes. In the second, a binary black hole system with non-spinning, equal mass black holes was placed inside a cosmological bubble; as a control, this system was also placed in vacuum. In the *Maya* code, all quantities are given in units of mass, where $M \approx 1$. The scalar field is dimensionless.

6.1 Cosmological Bubbles

First, we run two simulations of cosmological bubbles with no black holes. For both simulations, the same value of ϕ_0, the initial value inside the bubble, was used. This value was $\phi_0 = 0.05$. The first bubble had a radius of $r = 15M$, and the second had a radius of $r = 55M$. These scalar field parameters, in addition to wall thickness, are shown in Table 6.1. For both bubbles, the potential was set to zero everywhere. This zero-potential system causes critical collapse of the scalar field.

For both bubbles, a similar evolution is seen. First, the bubble shrinks while a thin shell of scalar field moves outward. As the bubble collapses inward, a trough of negative scalar field grows between the bubble and the expanding shell. Then, the bubble shrinks to a very small point at the origin. At this point, the scalar field becomes very negative ($\phi \approx -0.5, -0.8$ for the small and large bubbles, respectively).

ϕ_0	Radius	Thickness, σ	M_f	ADM Mass (M)
0.05	15	1	0.47080	1.22722
0.05	55	4	1.37352	4.29017

Table 1: Initial scalar field parameters and resultant black hole masses for cosmological bubbles.

The scalar field then "bounces back", with a diffuse bubble-type structure reappearing and expanding outward. This expands and diffuses until the scalar field settles to zero. Due to their similarity, the evolution is shown for only the small scalar field bubble in Figure 6.1.

In addition to the scalar field, the lapse scalar, α, is shown. As the bubble collapses, the lapse also collapses to zero, indicating the prescence of a black hole. The evolution of the lapse is shown with the scalar field evolution.

The resultant black hole has different mass for the two bubbles. The small bubble has a final mass of $M_f = 0.47080M$, while the large bubble's black hole is more than twice as massive with $M_f = 1.37352M$. This is expected as the large bubble has more mass-energy due to the greater surface area of the energetic wall.

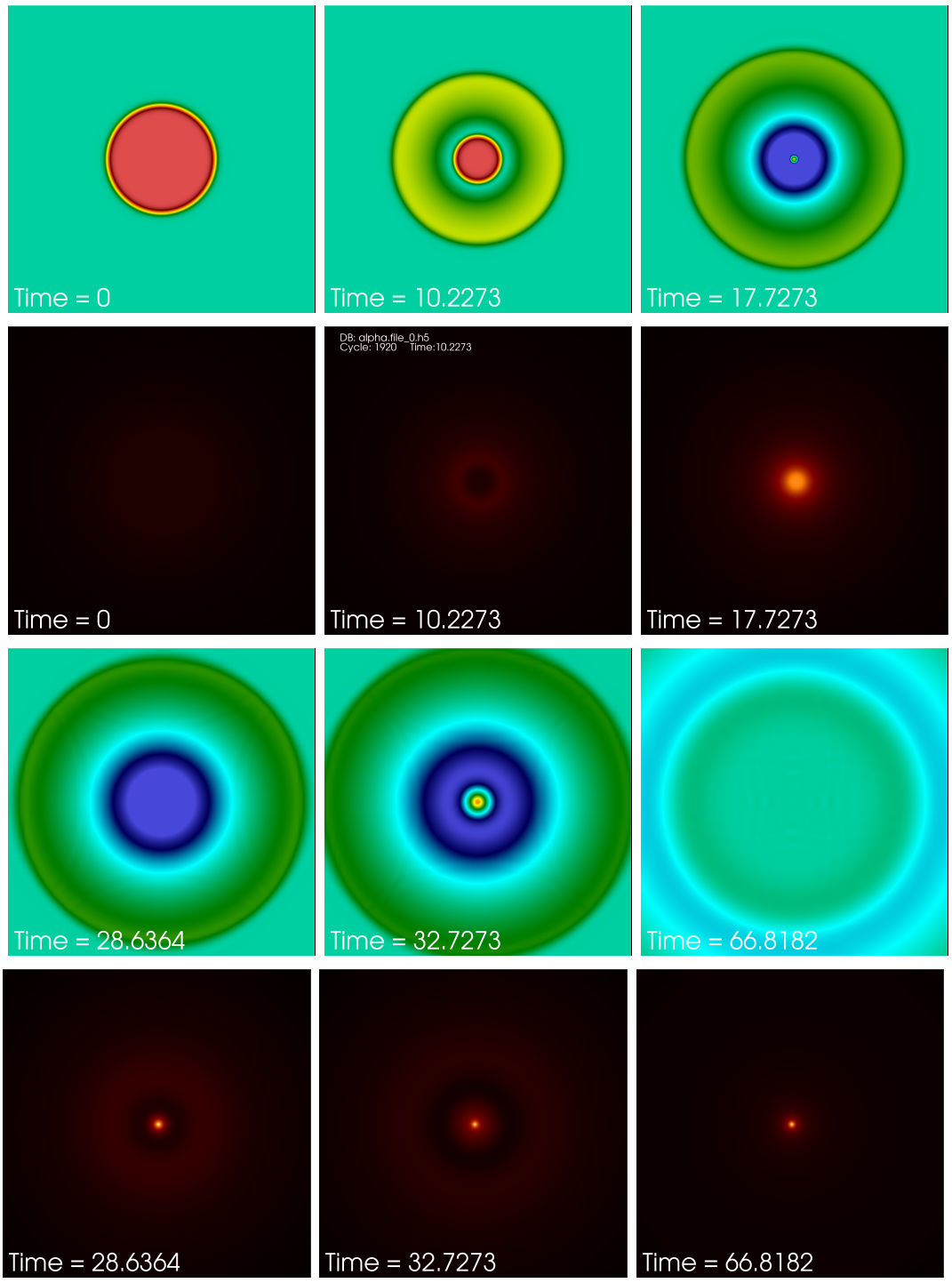

Figure 8: Two-dimensional slices of scalar field value, ϕ, in the xy-plane as the small scalar field bubble collapses is shown in rows 1 and 3 . Below each scalar field frame, in rows 2 and 4, is the corresponding xy-slices of the lapse, α. For the scalar field, the color bar is pinned to have a min/max of $0.055/-0.025$. The lapse is pinned between 0 and 1, with white corresponding to zero. The horizon of the black hole is first detected at $t = 50.5M$.

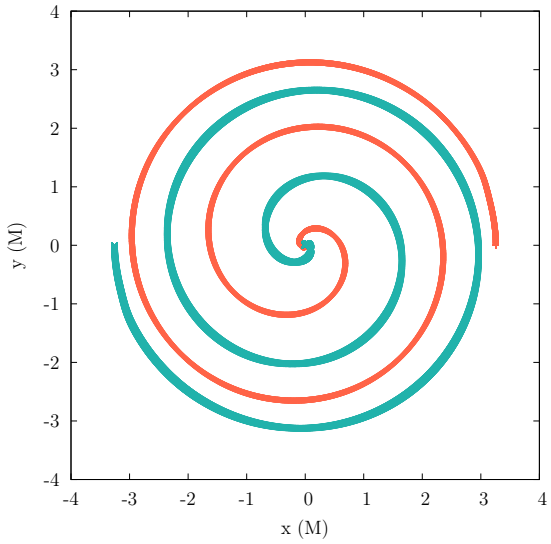

Figure 9: The black hole trajectories in vacuum.

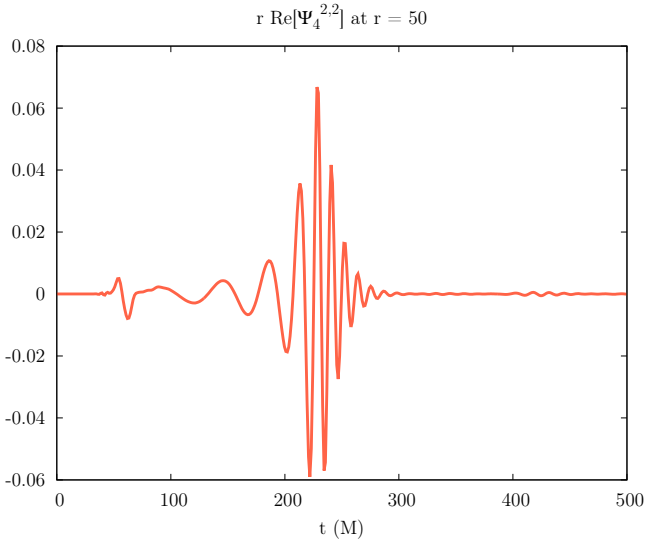

Figure 10: The waveform in vacuum.

6.2 Black Holes Embedded in Cosmological Bubbles

6.2.1 Vacuum

First, we will discuss the binary black hole merger in vacuum. The black holes are equal mass ($m = 0.453M$), have no initial spin, orbit in the xy-plane, and have an initial separation of $d = 6.514M$. An identical binary system was used in every

simulation. This system was based on the R1 system described by Baker et al [4].

The trajectories of the two black holes in the xy-plane as they merge is shown in Figure 9, and the waveform is shown in Figure 10. The waveform is multiplied by the radius at which it is extracted.

6.2.2 Binary black hole system inside a small radius cosmological bubble

For the bubble with small radius, $r = 15M$, two different values of ϕ_0 were tested. The first matched the corresponding bubble simulation from Section 6.1, and the second had a lower value of $\phi_0 = 0.01$. We begin with the larger scalar field value.

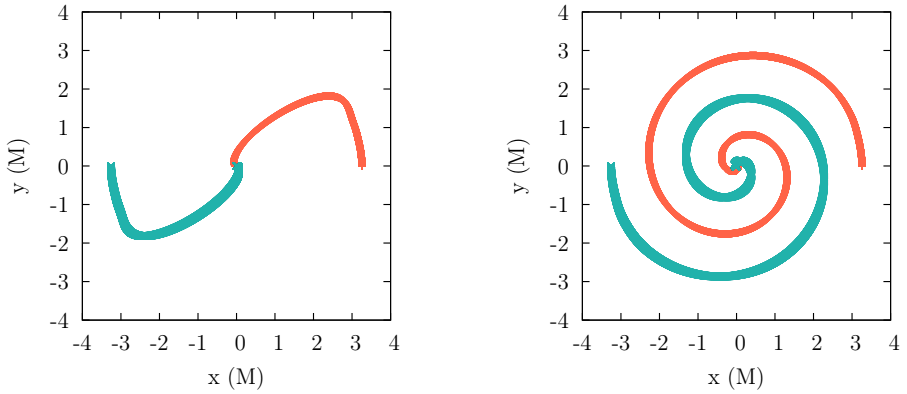

Figure 11: Black hole trajectories for black holes inside small radius cosmolgical bubbles. The initial scalar field value is $\phi_0 = 0.05$ on the left and $\phi_0 = 0.01$ on the right.

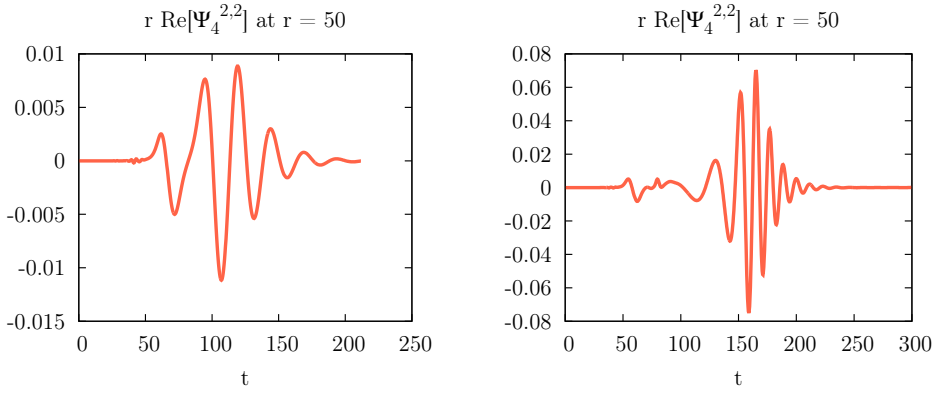

Figure 12: Waveforms for the BBH system inside small radius cosmolgical bubbles. The initial scalar field value is $\phi_0 = 0.05$ on the left and $\phi_0 = 0.01$ on the right.

6.2.2.1 *High initial scalar field value,* $\phi_0 = 0.05$

In the system with the larger initial scalar field value, the black holes accrete mass very quickly. The mass remains constant until $t \approx 20M$, where the binary accretes mass at a nearly linear rate before merger occurs. The resultant black hole mass is $M_f = 1.6143M$, nearly twice the mass of the black hole produced in vacuum.

Instead of a circular, inspiraling path, the black holes plunge towards each other. This is clearly seen in Figure 16(a), where the trajectories are plotted.

The evolution of the system is shown in detail in Figure 13. The bubble collapses around the binary and begins to warp into an oblong shape before thinning and collapsing. The third horizon appears at $t = 51.8182M$ (shown in Figure 13(e)). Then, the scalar field dissipates as a diffuse shell expands outward, similar to the behavior seen in the bubble-only system (Section 6.1).

The waveform is shown in Figure 12(a) and has a lower amplitude than the waveform in vacuum (Figure 10). A similar waveform was found by Baker et al [3] for a plunging system.

6.2.2.2 *Low initial scalar field value,* $\phi_0 = 0.01$

For the system with lower scalar field, the black holes have a more circular orbit, but still merge more quickly than the vacuum case. As in the previous system, the bubble warps around the black hole. However, the strong negative stage and "bounce" seen in the bubble-only system appears. This bounce and expansion are warped similar to the inital collapse. Regions of high scalar field intensity follow behind the black holes (see Figure 15(d)) before the scalar field expands outward and diffuses. Inside the outward-diffusing shell, there are regions of high scalar field which also diffuse slowly.

The black holes accrete mass as the field collapses, but this accretion stops as the field diffuses. The accretion occurs in two stages: first, there is a very rapid accretion during collapse, followed by a slower rate of accretion during the bounce. The mass

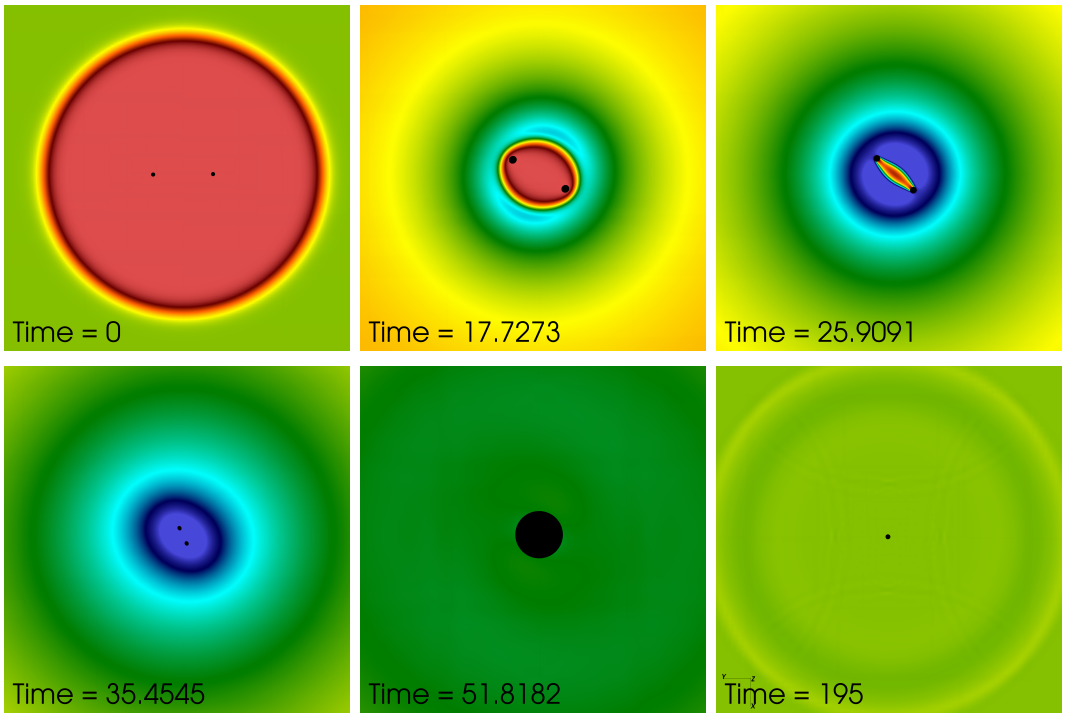

Figure 13: Two-dimensional slices of scalar field value, ϕ, in the xy-plane for a small, high-scalar field bubble showing the evolution of the scalar field with the binary inside. The color bar is pinned to have a min/max of -0.05/+0.05. The final frame shows a zoomed-out version of the system.

of the black holes remains constant until merger occurs around $100M$, resulting in a black hole with $M_f = 0.9005M$.

The waveform for this system is shown in Figure 12(b). By eye, the waveform appears similar to the vacuum waveform, but the waveform is produced earlier in time (due to the merger occurring more quickly). The comparison between this waveform and the vacuum waveform will be discussed in more detail in Section 6.2.4.

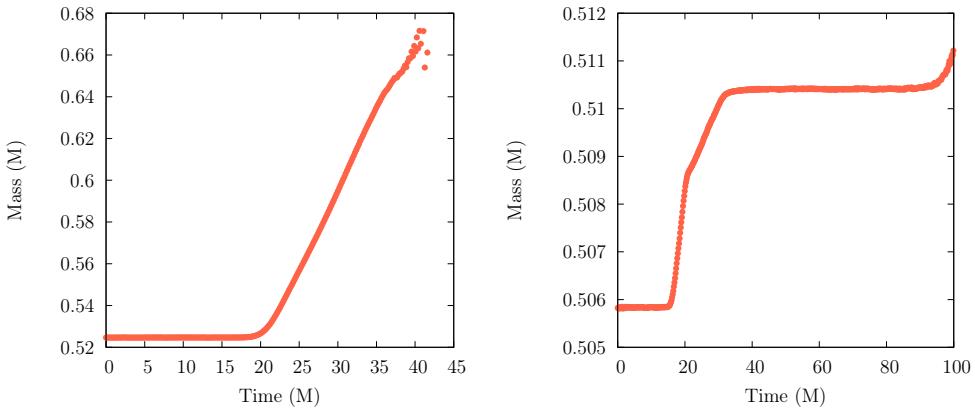

Figure 14: The mass as a function of time is shown for both initial scalar field values, with the larger value shown on the left.

6.2.3 Binary black hole system in a large radius cosmological bubble

As in the previous section, two values of the inital scalar field are investigated. In this system, the cosmological bubble has a radius of $r = 55$. Again, one matches the bubble-only simulation, and one has a much lower value.

6.2.3.1 High initial scalar field, $\phi_0 = 0.05$

In this system, the bubble collapses and becomes warped as seen previously. However, this warping does not occur until the bubble has almost completely reached the binary system. As in previous simulations, a trough of negative scalar field appears around the collapsing bubble. In this system, the negative-valued region is quite large and is maintained for nearly $40M$. Finally, the scalar field again becomes positive, expands,

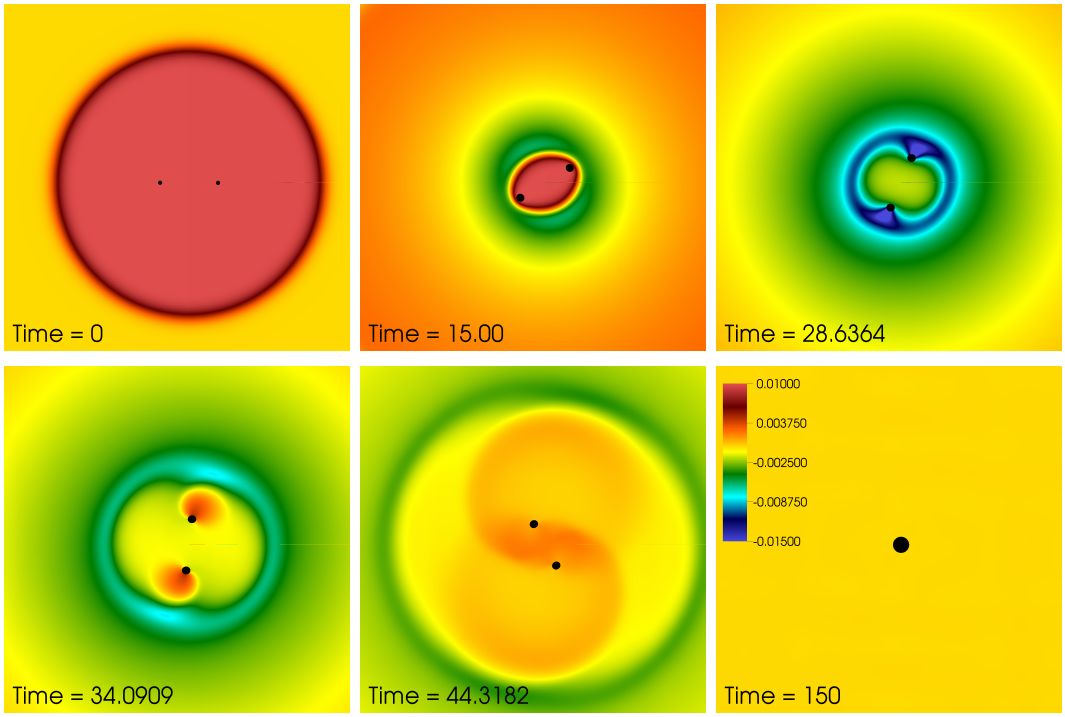

Figure 15: Two-dimensionals slices of scalar field value, ϕ, in the xy-plane as the small scalar field bubble with $\phi_0 = 0.01$ collapses around the black hole binary. The black hole horizons are shown in black. The colorbar min/max values are 0.01/-0.015.

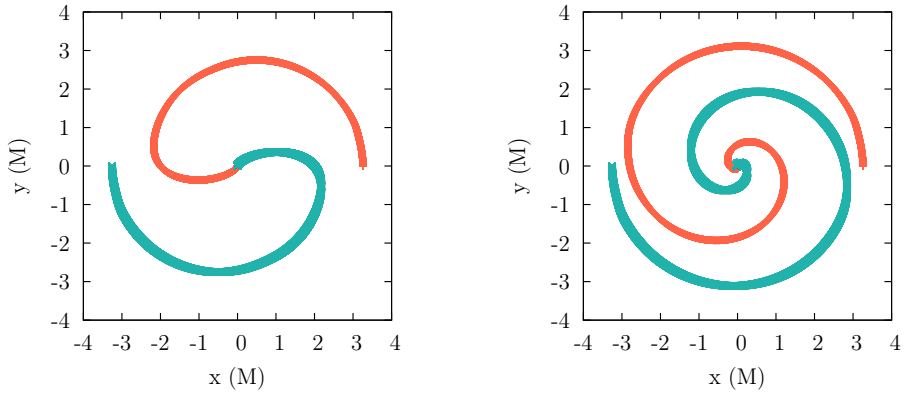

Figure 16: Black hole trajectories for black holes inside large radius cosmolgical bubbles. The initial scalar field value is $\phi_0 = 0.05$ on the left and $\phi_0 = 0.01$ on the right.

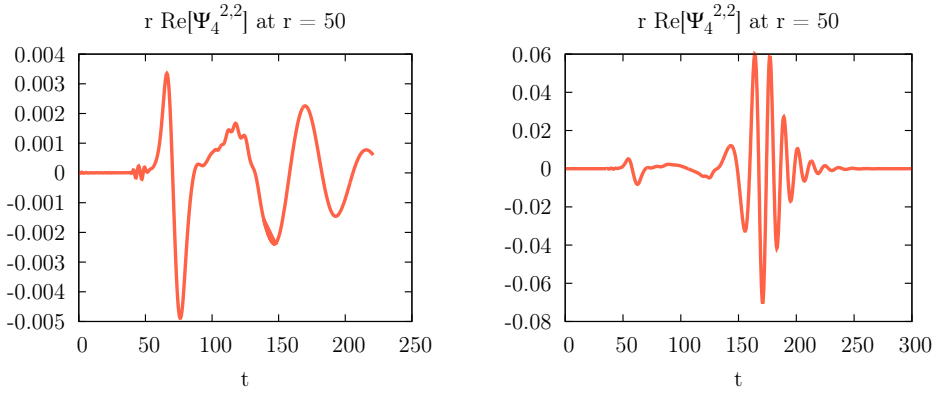

Figure 17: Waveforms for the BBH system inside the large radius cosmolgical bubbles. The initial scalar field value is $\phi_0 = 0.05$ on the left and $\phi_0 = 0.01$ on the right.

and dissipates. The apparent horizon of the merged black hole appears at $t = 102M$, before the scalar field "bounces" back.

The black hole trajectories in the large, high-scalar field system continue along their circular orbits for a longer period than the smaller bubble system before breaking into a plunge. The black holes complete nearly half an orbit before colliding nearly head-on; these trajectories are shown in Figure 16(a). This head-on collision behavior is also seen in the waveform, (Figure 17(a)). The accretion behavior of this system is shown in Figure 19(a). The mass stays constant until a rapid spike occurs just before merger. The final mass of the newly-formed black hole is $M_f = 1.7704$.

The waveform is shown in Figure 17(a); the waveform has a low magnitude and has a pronounced difference in shape than the vacuum or low scalar field waveforms. This difference is most likely due to the highly eccentric nature of the orbits.

6.2.3.2 Low initial scalar field, $\phi_0 = 0.01$

The evolution of the large bubble with a low initial scalar field is similar to the evolution of the small, low scalar field value; this evolution is shown in Figure 20. The bubble collapses around the binary, but the warping of the collapsed bubble is not as defined as in previous simulations. The slightly-warped shrinked bubble

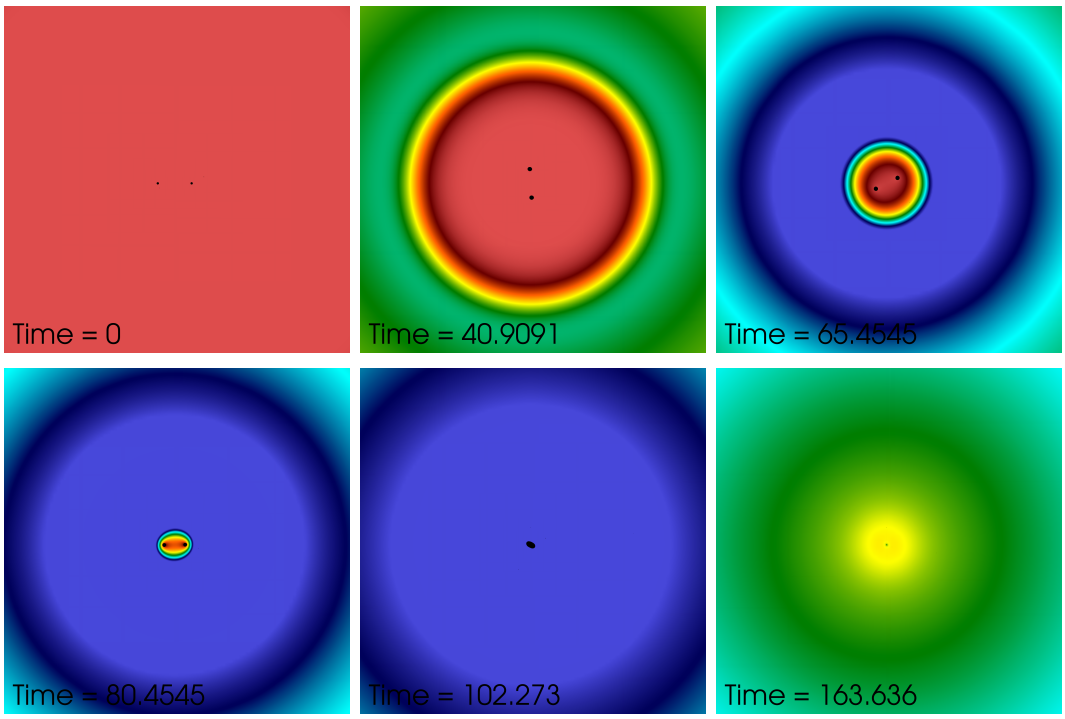

Figure 18: Two-dimensional slices of scalar field value, ϕ, in the xy-plane for a large, high-scalar field bubble showing the evolution of the scalar field with the binary inside. The binary is shown inside the bubble to highlight detail. In the first frame, the field of view is entirely inside the bubble. The color bar is pinned to have a min/max of -0.05/+0.05.

disappears into a field of negative scalar field before the field reappears and expands. As seen in the small scalar field bubble in Figure 15(d) (and in this system in Figure 20(d)), regions of high scalar field appear behind the horizons as they orbit in the expanding shell. Then, the field expands outward and becomes more diffuse before reaching a constant value.

The mass of the black holes as a function of time is shown in Figure 19(b). As seen in Section 6.2.2.2, the mass accretes in two stages. The first stage occurs as the bubble collapses, and the second stage occurs during the initial reappearance of the scalar field. The final mass of the resultant black hole is $M_f = 0.9251$.

In Figure 17(b), the waveform is shown. The amplitude of ψ_4 is slightly lower than seen in the matching small bubble simulation, but the shape is similar.

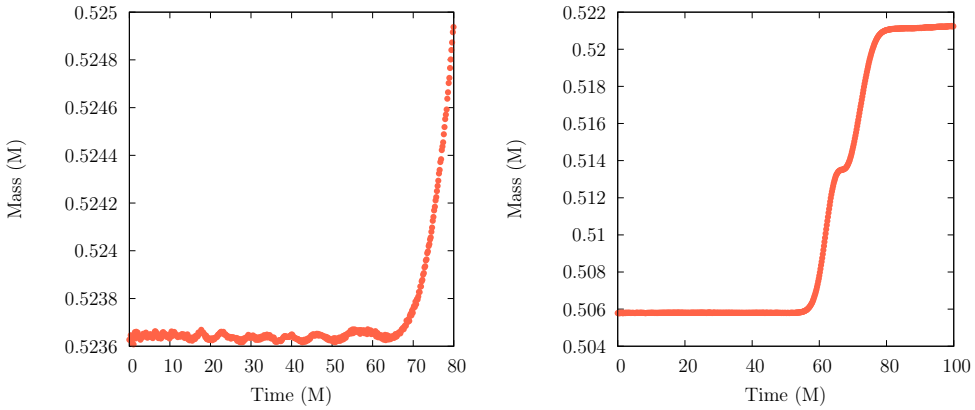

Figure 19: The mass as a function of time is shown for both initial scalar field values, with a high scalar field, $\phi_0 = 0.05$ on the left and the lower, $\phi_0 = 0.01$ on the right.

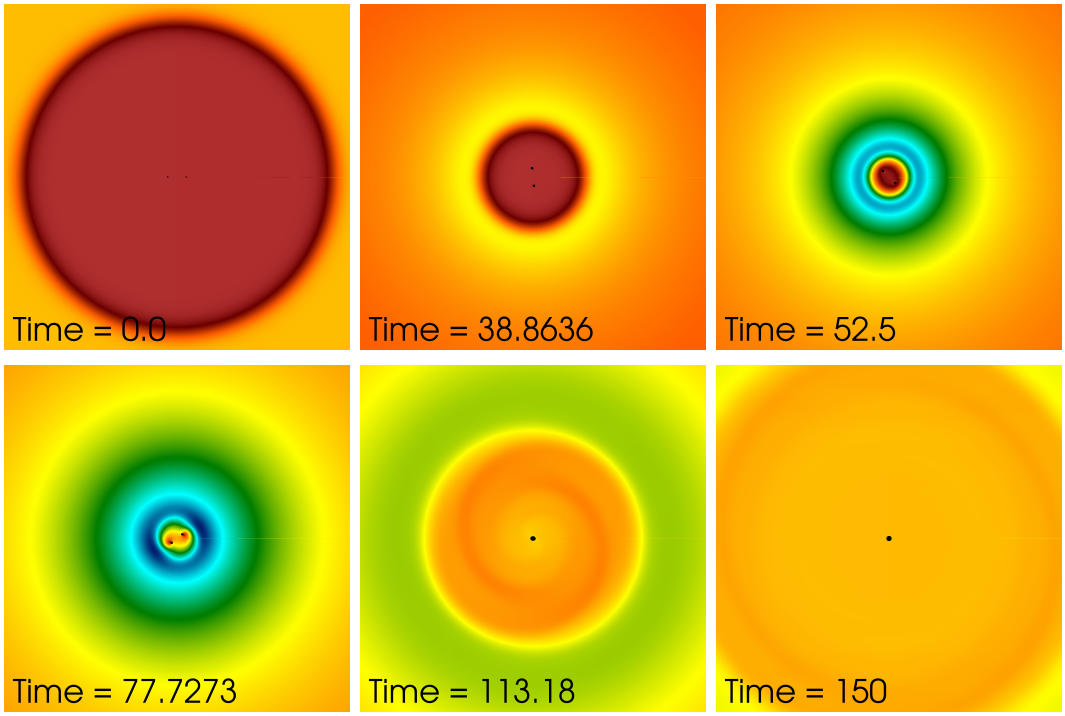

Figure 20: Two-dimensionals slices of scalar field value, ϕ, in the xy-plane as the large scalar field bubble collapses around the black hole binary. The black holes horizons are shown in black. The colorbar has been pinned to a min/max = -0.02/0.12.

Run type	ϕ_0	Bubble radius (M)	$M_f(M)$	S_z/M^2	ADM Mass (M)
Vacuum	n/a	n/a	0.8932	0.6276	0.995703
Bubble	0.01	15	0.9005	0.6548	1.04416
Bubble	0.01	55	0.9251	0.6893	1.16671
Bubble	0.05	15	1.6143	0.8306	2.25395
Bubble	0.05	55	1.7704	0.8427	5.43041

Table 2: Final black hole parameters for each binary simulation. For each run, the spin is only non-zero in the z-direction, so only the z-component, S_z, is listed.

6.2.4 Comparison

In Table 2, the resultant black hole characterstics are summarized. It is clear that both the size of the bubble and the intensity of the initial scalar field has an impact on the resultant mass and spin of the black holes. The largest effect was seen in the large, high scalar field bubble, which nearly doubled the mass of the vacuum case. As the mass increases, the resultant spin also increases. While the lower scalar field value bubbles displayed a less dramatic increase in mass and spin, the trajectories and waveforms were still effected.

In the Figure 21, the waveforms for the vacuum and lower scalar field bubbles are shown. Due to the irregular nature of the high scalar field value waveforms, they were not included.

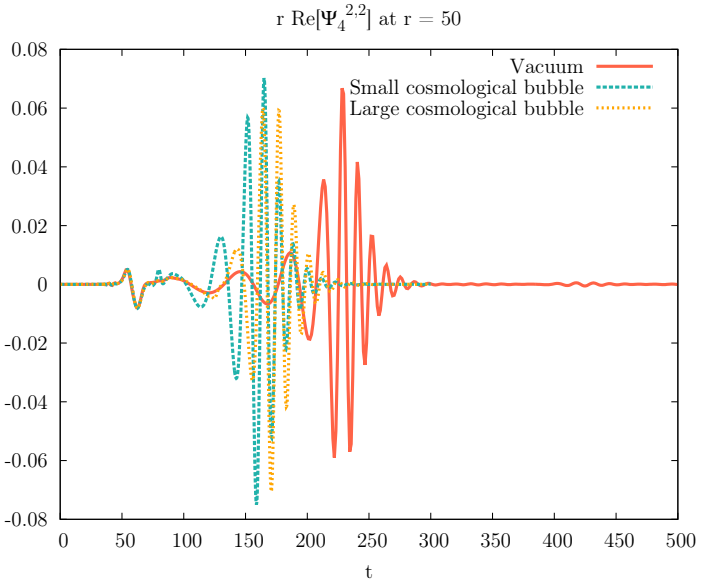

Figure 21: Comparison of waveforms in low scalar field bubbles and vacuum.

CHAPTER VII

CONCLUSIONS AND FUTURE WORK

In this work, we have examined the evolution of cosmological bubbles, both alone and with binary black holes. This was completed using the Einstein Toolkit and *Maya*, both scientific codebases that are well-suited for supercomputers.

It is possible that primordial black holes were created during scalar field collapse, or by another mechanism, during inflation. These black holes may have formed binaries within another scalar field bubble. As noted earlier, the simulations in this work are very fine-tuned. The scalar field bubbles are centered exactly at the center of mass of the black holes. Additionally, the initial scalar field value must be carefully chosen to ensure the black holes accrete while still maintaining circular orbits.

In future work, it may be interesting to place the black hole binaries in different regions of the scalar field bubbles. In order to model conditions during an inflationary period, a non-vanishing potential should be used. This problem is difficult due to the amount of mass-energy introduced to the system, making it numerically unstable. Another interesting direction for this work would be to use the LIGO data analysis pipeline to explore the possible parameter space of our waveforms.

REFERENCES

[1] Alcubierre, M., *Introduction to 3+ 1 Numerical Relativity*. Oxford University Press, 2008.

[2] Allen, G., Benger, W., Goodale, T., Hege, H. C., Lanfermann, G., Merzky, A., Radke, T., Seidel, E., and Shalf, J., "The cactus code: a problem solving environment for the grid," in *High-Performance Distributed Computing, 2000. Proceedings. The Ninth International Symposium on*, pp. 253–260, 2000.

[3] Baker, J., Brügmann, B., Campanelli, M., Lousto, C. O., and Takahashi, R., "Plunge waveforms from inspiralling binary black holes," *Physical review letters*, vol. 87, no. 12, p. 121103, 2001.

[4] Baker, J. G., Centrella, J., Choi, D.-I., Koppitz, M., and van Meter, J., "Binary black hole merger dynamics and waveforms," *Phys. Rev. D*, vol. 73, p. 104002, May 2006.

[5] Baumgarte, T. and Shapiro, S., *Numerical Relativity: Solving Einstein's Equations on the Computer*. Cambridge University Press, 2010.

[6] Berger, M. J. and Oliger, J., "Adaptive mesh refinement for hyperbolic partial differential equations," *Journal of Computational Physics*, vol. 53, no. 3, pp. 484–512, 1984.

[7] Choptuik, M. W., "Universality and scaling in gravitational collapse of a massless scalar field," *Physical Review Letters*, vol. 70, no. 1, p. 9, 1993.

[8] Guth, A. H., "Inflationary universe: A possible solution to the horizon and flatness problems," *Physical Review D*, vol. 23, no. 2, p. 347, 1981.

[9] Hall, L. J. and Hsu, S. D., "Cosmological production of black holes," *Physical review letters*, vol. 64, no. 24, p. 2848, 1990.

[10] Hawking, S. W., Moss, I. G., and Stewart, J. M., "Bubble collisions in the very early universe," *Phys. Rev. D*, vol. 26, pp. 2681–2693, Nov 1982.

[11] Husa, S., Hinder, I., and Lechner, C., "Kranc: a mathematica package to generate numerical codes for tensorial evolution equations," *Computer Physics Communications*, vol. 174, no. 12, pp. 983–1004, 2006.

[12] Johnson, M. C., Peiris, H. V., and Lehner, L., "Determining the outcome of cosmic bubble collisions in full general relativity," *Physical Review D*, vol. 85, no. 8, p. 083516, 2012.

[13] Kolb, E. and Turner, M., *The Early Universe*. Addison-Wesley Publishing Company, 1990.

[14] Liddle, A. and Lyth, D., *Cosmological Inflation and Large-Scale Structure*. Cambridge University Press, 2000.

[15] Mo, H., Van den Bosch, F., and White, S., *Galaxy formation and evolution*. Cambridge University Press, 2010.

[16] Newman, E. and Penrose, R., "An approach to gravitational radiation by a method of spin coefficients," *Journal of Mathematical Physics*, vol. 3, no. 3, pp. 566–578, 1962.

[17] Press, W. H., Teukolsky, S. A., Vetterling, W. T., and Flannery, B. P., *Numerical recipes in C*, vol. 2. Cambridge University Press, 1996.

[18] S.Carroll, *Spacetime and Geometry: An Introduction to General Relativity*. Addison Wesley, 2004.

[19] Schnetter, E., Hawley, S. H., and Hawke, I., "Evolutions in 3d numerical relativity using fixed mesh refinement," *Classical and Quantum Gravity*, vol. 21, no. 6, p. 1465, 2004.

[20] Turner, M. S., Weinberg, E. J., and Widrow, L. M., "Bubble nucleation in first-order inflation and other cosmological phase transitions," *Phys. Rev. D*, vol. 46, pp. 2384–2403, Sep 1992.

[21] Zilhão, M. and Löffler, F., "An introduction to the einstein toolkit," *International Journal of Modern Physics A*, vol. 28, no. 22n23, p. 1340014, 2013.